Prepublished copy

Nature Environment & Pollution Technology

This is a peer-reviewed prepublished version of the paper to be published in Vol. 25, No. 2, June 2026 issue

Original Research

Synthesis and Adsorptive Performance of Zn/Al Dually Doped *Brassica oleracea var. italica* Stem Nanocomposite: Insights from RSM Optimization

Yagna Sri Thikkada[1], Alpitha Suhasini Juttuka[2], Venkata Ramana Avula[3], NagaRaju Yendluri[4], Kapavarapu Sreekar[5], Pulipati King[6] and Meena Vangalapati[7*]

[1,4,5,6,7] Department of Chemical Engineering, AUCE, Andhra University, Visakhapatnam, AP

[2] Department of Chemical Engineering and Petroleum Engineering, UCEK, JNTUK, Kakinada, AP

[3] Department of Petroleum Engineering, Godavari Global University, Rajahmundry, AP

[*]Corresponding author, e-mail: meenasekhar2002@yahoo.com

ORCID IDs: Yagna Sri Thikkada: https://orcid.org/0009-0001-0009-7653

Alpitha Suhasini Juttuka: https://orcid.org/0000-0002-5399-2635

Venkata Ramana Avula: https://orcid.org/0000-0001-9496-6129

NagaRaju Yendluri: https://orcid.org/0009-0006-2715-292X

Kapavarapu Sreekar: https://orcid.org/0009-0006-9510-8680

Pulipati King: https://orcid.org/0000-0001-8210-3019

Meena Vangalapati: https://orcid.org/0000-0002-7303-8160

Key Words	Zn/Al dually doped nanocomposite, *Brassica oleracea* var. *italica*, Sustainable nanocomposite, Structural and surface features, Dye adsorption, RSM with a CCD
DOI	https://doi.org/10.46488/NEPT.2026.v25i02.B4379 (DOI will be active only after the final publication of the paper)
Citation for the Paper	Thikkada, Y.S., Juttuka, A.S., Avula, V.R., Yendluri, N., Sreekar, K., King, P. and Vangalapati, M., 2026. Synthesis and adsorptive performance of Zn/Al dually doped *Brassica oleracea var. italica* stem nanocomposite: insights from RSM optimization. *Nature Environment and Pollution Technology*, 25(2), B4379. https://doi.org/10.46488/NEPT.2026.v25i02.B4379

ABSTRACT

In this study, a sustainable nanocomposite was synthesized using stem waste of Brassica oleracea var. italica, dually doped with zinc and aluminum (Zn/Al@BOI), through a chemical co-precipitation method. The material was designed for the efficient adsorptive treatment of wastewater to remove Malachite Green (MG). Structural and surface features were analyzed using approaches such as SEM, BET, EDX, XRD, FTIR, XPS, and TGA. The presence of Zn and Al was confirmed by EDX and XPS, while BET surface area analysis confirmed a notably high value of 80.53 m^2/g, suggesting the material's strong capability for adsorption. To investigate its adsorption behavior, a set of batch tests were carried out, focusing on the influence of time, pH, adsorbent dose, MG dye concentration, and temperature. Using RSM with a CCD, the ideal operational conditions were determined to be approximately 29.64 minutes of contact time, 0.29 g/L dosage, pH 7.96, and 20 ppm dye concentration, resulting in a greater efficiency of 97.31%. Equilibrium data best fit the Freundlich isotherm (R^2 = 0.9957), while the Langmuir model analysis revealed a monolayer capacity of 336 mg. g^{-1}.

The adsorption kinetics were effectively represented by the pseudo-2nd-order model and thermodynamic findings revealed a spontaneous, endothermic, and, physisorption-driven process.

INTRODUCTION

The issue of water pollution is particularly relevant when it arises from industrial sources such as dye effluents, as it can have dire consequences for posing serious risks to both environmental and human well-being (Sowjanya et al. 2023). Contaminated waters from the textile, leather, and paper industries are major environmental concerns because they discharge synthetic dyes such as MG, which are non-biodegradable, toxic, and persistent (Raval et al. 2017). Malachite Green ($C_{23}H_{25}ClN_2$), widely used in textile industries and aquaculture, is a clear example, as it is a synthetic dye with strong color and chemical stability. Its complex molecular structure makes it toxic, environmentally resistant, and biodegradation-resistant (Varma et al. 2020). The dye's accumulation in aquatic systems endangers the environment and human health, therefore stringent policies are needed alongside effective removal strategies (Shindhal et al. 2021). Adsorption is regarded as one of the most efficient methods among those studied for —including photocatalysis, coagulation-flocculation, chemical oxidation, and membrane filtration—because of its operational ease, low cost, high efficacy even at low concentrations, and lack of harmful by-products (Inobeme et al. 2024, Dutta et al. 2021). These factors have made it increasingly favorable in recent years (Bilal et al. 2022).

Over the past few years, researchers have increasingly explored nanomaterial-based adsorbents because of their exceptionally large surface area, heightened chemical reactivity, and strong ability to bind with various pollutants (Zhang et al. 2022). One of the key applications of such materials is in addressing synthetic dye contamination in industrial liquid waste. The use of sustainable, bio-waste-derived nanocomposites has become increasingly prominent, particularly those doped with metals, which combine cost-effectiveness with environmental safety (Jha et al. 2024). The advancement of nanotechnology has enabled the fabrication of high-performance adsorbents with better selectivity, recyclability, and efficiency, making them highly suitable for and broader wastewater treatment applications (Granado et al. 2024).

Among bio-derived materials, agricultural and food-processing wastes stand out because they are inexpensive, widely available, and environmentally sustainable. When doped with metals such as Zn, Al, Fe, Ti, Mn, Co, Ni, Ag, and Cu, these wastes can be transformed into efficient adsorbents with improved porosity and active surface sites. Several studies have demonstrated the utility of such materials synthesized through green routes. For instance, Cifci et al. (2022) explored iron-doped coffee waste applied as a low-expense solution for capturing Reactive Blue 21 dye, presenting an innovative reuse of food waste. Manoj Kumar et al. (2023) synthesized ZnO nanoparticles using Brassica oleracea var. botrytis (cauliflower) leaf extract via a co-precipitation method, promoting plant-based synthesis. Similarly, Ananda et al. (2023) employed Basella alba leaf juice in the combustion synthesis of $2ZrO_2$–$7ZnO$ nanoparticles, and Ashraf et al. (2023) used amla seed extract to green-synthesize iron oxide nanoparticles with enhanced biological compatibility.

Other notable examples include the fabrication of aluminum-doped cadmium oxide cathodes using plasma-treated peanut shell-derived carbon for energy storage systems (Karthikeyan et al. 2023) and the synthesis of zinc-doped hydroxyapatite nanorods from scallop shell waste for potential biomedical use (Karunakaran et al.

2023). These examples highlight the broad versatility of metal-doped, bio-waste-derived materials across environmental, biomedical, and energy sectors.

Recent advances in green chemistry further support the use of dually doped systems—where two metals are integrated into biomass matrices—to enhance adsorption efficiency. This strategy boosts surface reactivity, active site availability, and overall performance. Chan et al. (2020), for example, developed ZnO nanoparticles dually doped with Fe and Ag using Clitoria ternatea extract, achieving a 97.4% removal of Congo red. Velusamy et al. (2025) prepared a Ni/Al-layered double hydroxide (LDH) through neem-assisted co-precipitation that removed more than 95% of methylene blue dye. Ouadrhiri et al. (2022) reported the development of an N, P dually doped carbon catalyst from olive pomace, capable of degrading 94.6% of methyl orange through persulfate-assisted oxidation. Mohan Raj et al. (2023) introduced a novel composite material, [EDA-OPDA] Al@Zn, by coating aluminum with a copolymer and then incorporating zinc via electrodeposition—showcasing the adaptability of metal dually doping approaches.

Given the increasing focus on sustainable water treatment, dually doping bio-waste with metals like Zn and Al, especially in biomass like Brassica oleracea stems (found in broccoli, cabbage, and cauliflower), has shown to significantly improve porosity, functional group density, and adsorption affinity. Building on this, the current stud on the eco-friendly fabrication of a Zn/Al dually doped nanocomposite (Zn/Al@BOI) using Brassica oleracea var. italica (broccoli) stem waste via a simple chemical co-precipitation method. This environmentally friendly process avoids hazardous reagents and supports promoting sustainability in chemistry by repurposing agricultural waste. The nanocomposite was effectively utilized to treatment of wastewater to remove Malachite Green (MG). Its structural and surface activity were thoroughly examined employing methods like SEM-EDX, XRD, BET, FTIR, and TGA, all of which confirmed successful metal incorporation and a favorable surface morphology. To evaluate its adsorption behavior, batch experiments were carried out under varying conditions of contact time, adsorbent dosage, dye concentration, temperature, and, pH. The adsorption mechanism was further explored through isotherm, kinetic, and thermodynamic models. For process optimization, RSM(ResponseSurface Methodology) using a CCD(Central Composite Design) was utilized to determine the most effective operating variables. The nanocomposite showed high removal efficiency even in real wastewater conditions, underscoring its promise as a sustainable and effective adsorbent for dye remediation.

1. MATERIALS AND METHODS

2.1. Materials

$ZnCl_2$, Al_2O_3, Triton X-100, sodium hydroxide (NaOH) pellets, MG dye, and DI water were procured from Andhra Scientific Agency, Kakinada, India. Stems of *Brassica oleracea var. italica* was collected from vegetable market, Kakinada, India.

2.2. Preparation of Brassica oleracea var. italica stems powder

The stems were first rinsed extensively with distilled water to eliminate surface contaminants and impurities. They were chopped into smaller pieces and left to dry naturally in sunlight for four days. It was then placed in an oven at 70 °C for 12 hours to achieve total dehydration. Once dried, the material was finely ground

and passed through a 100-mesh (150 µm) sieve to achieve a consistent powder, which was then stored in sealed containers for later use in synthesizing the nanocomposite (Granado et al. 2024).

2.3. Selection of Zn: Al ratio

A Zn to Al molar ratio of 2:1 was chosen for synthesizing the Zn/Al@BOI nanocomposite to balance surface reactivity and structural stability. This ratio is supported by literature indicating that moderate zinc enrichment improves ZnO dispersion, enhances active site density, and boosts adsorption efficiency. Higher ratios (e.g. 3:1) may cause Zn agglomeration and reduced surface area, while lower ratios (e.g. 1:1 or 1:2) could limit Zn^{2+} availability essential for dye interaction. Thus, the 2:1 ratio offers an optimal composition for developing a porous, metal-rich, and stable adsorbent for aqueous (Ouassif et al. 2020, Tajat et al. 2022, Youssef et al. 2017).

2.4. Preparation of Zn/Al@BOI nanocomposite

A sustainable Zn/Al@BOI nanocomposite was prepared using 20 g of dried, powdered *Brassica oleracea* var. *italica* biomass via co-precipitation and calcination (Fig. 1). The biomass was stirred into 200 mL of distilled water to ensure uniform dispersion. Zinc chloride and aluminum chloride hexahydrate (0.5 M each) were added in a Zinc and Al molar ratio of 2:1 to enhance structural stability and adsorption efficiency (Youssef et al. 2017). To control particle size and dispersion, 1 g of Triton X-100 was introduced. The prepared metal salt solution was gradually added dropwise into the biomass suspension while continuously stirring, and the pH was carefully regulated to pH 10 using NaOH to initiate the co-precipitation process. The mixture was heated at 70 °C with continuous stirring for 3 hours, then left to stand at room temperature for 24 hours. The solid formed was filtered out, washed with distilled water until the pH became neutral, and then dried in an oven at 80 °C for 12 hours. To enhance crystallinity and stability, the dried material was subsequently calcined at 450 °C for 3 hours to form stable metal oxides with improved crystallinity and surface activity. (Velusamy et al. 2025, Ouadhriri F et al. 2022, Ouassif et al. 2020).

Fig. 1: Overview of the synthetic route used to prepare the Zn/Al@BOI nanocomposite

2.5. Batch Mode Adsorption Tests

Adsorption experiments were conducted by systematically varying key parameters, including treatment time, nanocomposite dose (g/L), pH, and MG dye concentration (mg/L). The prepared dye-adsorbent mixtures were shaken using an orbital shaker with temperature control for predetermined time intervals. Post-agitation, centrifugation was performed at 4000 rpm for 15 minutes to achieve phase separation. The concentration of unabsorbed dye in the liquid phase was quantified using UV–Visible spectroscopy at 618 nm, employing a 1 cm quartz cuvette. The pH of the solutions was monitored using a calibrated digital pH meter (Sowjanya et al. 2023, Ratnam et al. 2022, Subhashita et al. 2022). The % removal was determined according to equation (1) and the equilibrium uptake of dye by the adsorbent (q_e, mg/g), which indicates the quantity of MG dye retained per gram of adsorbent at equilibrium according to equation (2):

$$\% \text{ Removal efficiency} = \frac{C_o - C_e}{C_o} \times 100 \quad (1)$$

$$\text{Dye uptake} = (C_o - C_e) \times \frac{V}{m} \quad (2)$$

Here, C_o and C_e correspond to the MG concentrations at the beginning and at equilibrium (mg/L), V is the solution volume in liters, and m denotes the amount of adsorbent in grams.

2.6. Isotherm, Kinetic and Thermodynamic Studies

Equilibrium adsorption studies are essential for understanding both the capacity of the nanocomposite and the nature of its binding with dye molecules. In this work, the adsorption behavior of MG onto the Zn/Al@BOI nanocomposite was assessed through two well-established models, the isotherm models of Langmuir and Freundlich. The Langmuir describes monolayer coverage on an even surface possessing identical and fixed adsorption sites, while the Freundlich model is empirical in nature and describes adsorption on uneven surfaces with sites of different binding strengths. The corresponding mathematical expressions for these models are presented in Equations (3) and (4) (Sowjanya et al. 2023; Ratnam et al. 2022; Subhashita et al. 2022). The following equation outlines the Langmuir (Eq. 3) and Freundlich (Eq. 4) adsorption isotherm:

$$\frac{C_e}{q_e} = \left(\frac{C_e}{q_{max.}}\right) + \frac{1}{q_{max.} . b} \quad (3)$$

$$\ln q_e = \ln K_f + \frac{1}{n} \ln C_e \quad (4)$$

In this equation, q_{max} represents the maximum amount of dye that can be adsorbed per unit mass of adsorbent (mg. g^{-1}), and b corresponds to the Langmuir constant related to adsorption affinity (L/mg). For the Freundlich model, the constants K_f and n correspond to the dye uptake and the absorbance of adsorption, indicating surface heterogeneity, respectively.

Kinetic models are useful for analyzing adsorption rates and determining rate-controlling mechanisms. In this work, the adsorption kinetics of MG onto Zn/Al@BOI nanocomposite were assessed using pseudo-1st order, pseudo-2nd order, Elovich and intra-particle diffusion models to describe the interaction dynamics between dye

molecules and the adsorbent surface (Subhashita et al. 2022, Ho et al. 1999, Debord et al. 2022, Dharmarathna et al. 2024). The mathematical equations of Pseudo first (Eq. 5) and second order (Eq. 6) kinetic models:

$$\ln(q_e - q) = -K_1 t + \ln q_e \quad (5)$$

$$\frac{t}{q} = \left(\frac{1}{q_e}\right) t + \left(\frac{1}{K_2} \cdot \frac{1}{q_e^2}\right) \quad (6)$$

Here, q_e (mg/g) is defined as the equilibrium concentration of MG dye adsorbed on one gram of the adsorbent, indicating the system's adsorption capacity. The term q_t (mg/g) denotes the dye uptake at a specific time t. K_1 and K_2 are represent the rate constants for the pseudo-first and -second order models, respectively, with units of 1/min and g/(mg·min), and used to describe the adsorption rate and underlying kinetics.

Adsorption behavior is closely linked to thermodynamic parameters like Gibbs free energy (ΔG°), enthalpy (ΔH°), and entropy (ΔS°), revealing its spontaneity, thermal behavior, and the level of randomness between the solid and liquid phases. These values are determined using the distribution coefficient (K_c), and calculated through temperature-dependent relationships, typically employing the Van't Hoff equation (Sowjanya et al. 2023, Ratnam et al. 2022, Subhashita et al. 2022).

$$\Delta G^o = -RT \ln K_c \quad (7)$$

$$K_c = \frac{q_e}{C_e} \quad (8)$$

$$\ln K_c = -\frac{\Delta H^0}{RT} + \frac{\Delta S^0}{R} \quad (9)$$

where T is the absolute temperature (K), R is the universal gas constant (8.314 $J \cdot mol^{-1} \cdot K^{-1}$), C_e (mg/L) is the equilibrium dye concentration, and q_e (mg/g) represents the amount of dye adsorbed at equilibrium.

2.7. RSM (Response Surface Methodology)

RSM is a powerful tool combining numerical modelling approaches to analyze experimental data, assess variable interactions, and develop predictive models (Sowjanya et al. 2023, Poiba et al. 2023, Polipalli et al. 2013). Among its designs, CCD (Central Composite Design) is widely used for process optimization, as it can estimate linear, quadratic, and interaction effects without compromising model reliability. CCD employs axial (star) points outside the factorial cube, maintaining uniform prediction accuracy around the centre point. In this study, preliminary screening identified suitable parameter ranges. CCD was used to optimize four measures: stirring time (A), adsorbent dose (B), pH (C), and adsorbate concentration (D). A second-order polynomial model was generated in Design Expert 13 to predict efficiency.

Table 1: Factors effecting on optimization

Factors	Units	Min (-1)	Max (+1)
A-Time	min	10.00	50.00
B-Dosage	g/L	0.10	0.50
C-pH		6.00	10.00

D-Concentation	mg/L	10.00	30.00

3. RESULTS AND DISCUSSION

3.1. Characterization of Adsorbent

The SEM image (Fig. 2a) revealed that the Zn/Al@BOI nanocomposite exhibited a distinct layered morphology with a nanoflake-like appearance. These structures appeared as irregularly shaped, aggregated sheets, suggesting the successful formation of a porous and interconnected network. Such morphology is advantageous for adsorption, as it offers enhanced surface area and large accessible active sites and the particle sizes observed in the micrograph ranged from 47.10 to 64.49 nm, confirming the nanoscale dimension of the synthesized material. This structural arrangement is consistent with typical lamellar morphologies observed in layered double hydroxide-based nanomaterials, further supporting the effective incorporation of Zn and Al into the biomass matrix. The loose, porous arrangement of the flakes suggests a high surface area with numerous accessible active sites, making the material well-suited for adsorption applications (Aziz et al. 2023, Javadian et al. 2014, Mall et al. 2006).

Elemental composition analyzed via EDX (Fig. 2b) revealed a dominant presence of carbon, oxygen, zinc, and aluminum, together accounting for approximately 92–94 wt.%, which forms the backbone of the nanocomposite. Additional elements such as sodium, potassium, calcium, phosphorus, and trace chlorine were also detected, likely originating from the biomass source or residual precursors like $ZnCl_2$ and $AlCl_3$, indicating that the washing process was effective (Sowjanya et al. 2022).

The XRD patterns (Fig. 2c) exhibited well-defined peaks at 2θ values of 32.1°, 34.0°, 36.2°, 48.3°, 57.1°, 63.6°, 66.1°, and 68.1°, which are indexed to the (100), (001), (101), (102), (103), (110), (200), and (112) planes of hexagonal wurtzite ZnO, confirming its crystalline phase. The broadening of peaks suggests the presence of nanocrystalline domains and possible lattice distortion due to Al^{3+} incorporation. These findings collectively confirm the successful formation of crystalline Zn/Al@BOI nanocomposites with surface and structural features highly favorable for adsorption processes (Banerjee et al. 2017; Klett et al. 2014).

The infrared FT-IR spectra of the Zn/Al@BOI nanocomposite before and after MG removal are mention in Fig. 3(a) and 3(b). Prior to adsorption, characteristic peaks were identified at 3420.17 cm^{-1}, 2923.88 cm^{-1} and 1630.64 cm^{-1}, likely due to H-O-H bending or C=O vibrational stretching modes. Additional signals at 1382.24 cm^{-1}($–CH_3$ bending) and 1026.74 cm^{-1}(C=O stretching) are observed, alongside lower-frequency bands at 876.32, 617.29, and 466.65 cm^{-1}, corresponding to C–H bending and metal–oxygen (Zn–O and Al–O) vibrational modes. After adsorption of MG dye, notable spectral changes occurred. The broad O–H band near 3420 cm^{-1} decreased in intensity and shifted slightly, suggesting hydrogen bonding or interaction with dye molecules. The peak at 1630.64 cm^{-1} became more pronounced, possibly due to aromatic C=C stretching or N–H bending vibrations introduced by the dye. Reductions in the 1382 and 1026 cm^{-1} bands indicated participation of $–CH_3$ and C-O groups in the adsorption. Additionally, a weakening of metal–oxygen vibrational bands below 700 cm^{-1} suggested surface interactions or coverage by MG dye molecules. These spectral modifications point to both physical and chemical adsorption mechanisms (Sowjanya et al. 2022; Elizalde et al. 2006; Parveen et al. 2018).

To explore the surface chemistry of Zn/Al@BOI, XPS analysis was performed. The full-range XPS scan (Fig. 4a) revealed the existence of C 1s (49.2%), O 1s (42.4%), Zn $2p_3$ (5.6%), Al 2p (2.7%), and trace Cl 2p

(<0.1%), confirming the material's elemental composition. High carbon and oxygen contents reflect the biomass origin and surface metal oxide formation. The C 1s spectrum (Fig. 4b) showed a primary peak at 285.1 eV (C–C/C–H) and a shoulder at 286.2 eV (C–O). The O1s spectrum (Fig. 4c) displayed peaks at 531.2 eV (Zn–O/Al–O) and 532.6 eV (OH^- or adsorbed oxygen). Zn 2p peaks at 1021.9 eV and 1044.9 eV (Fig. 4d) confirmed Zn^{2+} as ZnO, while the Al 2p signal at 74.3 eV (Fig. 4e) indicated Al^{3+} in Al_2O_3, consistent with values reported by Liu et al. (2019). These findings confirm the incorporation of Zn and Al, along with oxygen-containing groups that enhance.

The thermal behavior of the Zn/Al@BOI nanocomposite was evaluated through TGA, DTG, and DTA analyses (Fig. 5a–b). The TGA curve showed three main steps in mass loss. The preliminary loss of approximately 4.3% below 150 °C was linked to the release of physically adsorbed volatile water. Between 150–300 °C, a significant mass reduction of around 15.0% occurred, attributed to the decomposition of organic components, likely cellulose and other plant-based residues. Beyond 300 °C, a gradual mass reduction continued to 600 °C, primarily due to breakdown of residual organics and dehydroxylation of Zn and Al hydroxides. A DTG peak centered near 250 °C marked the primary decomposition stage, which aligned with a strong endothermic signal in the DTA curve. Overall, a total mass loss of about 18.3% was observed, suggesting moderate organic content in the material. The remaining mass (~81.7%) reflects high thermal stability and indicates the presence of thermally robust metal-oxides such as ZnO and Al_2O_3 within the composite structure (Monvisade et al. 2009; Li et al. 2018).

The porous structure of Zn/Al@BOI was further examined via nitrogen adsorption–desorption analysis (Fig. 6a–b). The isotherm manifested a Type IV pattern with a H3 loop in the relative pressure of $P/P_0 \approx 0.8–1.0$, Typical of mesoporous materials with slit-like pores, often found in layered composites. A sharp uptake at P/P_0 close to 1.0 indicates capillary condensation within mesopores. The BJH pore size distribution (Fig. 6b) showed a dominant average pore size of ~3.77 nm, alongside a broader range between 20–60 nm, which may result from interparticle voids or larger mesopores. The BET surface area was measured to be 80.53 $m^2 . g^{-1}$, with a 0.186 cm^3/g total pore volume. These properties imply high surface availability and effective pore diffusion pathways, making the composite well-suited for dye adsorption applications. The summarized data in Table 2 underscore its mesoporous nature and adsorption efficiency potential (Kacan et al. 2016; Naeem et al. 2022).

3.2. Batch Adsorptive Investigations

The adsorptive performance of the Zn/Al@BOI nanocomposite toward Malachite Green (MG) dye was systematically investigated by evaluating the influence of key operational parameters. In each set of experiments, one parameter was varied while maintaining others constant, ensuring a clear understanding of its individual impact and facilitating the determination of optimal adsorption conditions (Sowjanya et al. 2023; Ratnam et al. 2022). As mention in Fig. 7a, time-dependent behavior was examined under fixed conditions of pH-7, temperature-303 K, and nanocomposite dosage 0.4 g/L. A rapid rise in occurred during the initial phase in 30 min, which gradually plateaued, indicating the attainment of adsorption equilibrium. The rapid initial uptake is given the abundance of sorption sites on the adsorbent, which become occupied over time, slowing the adsorption rate. As time progressed, site saturation led to a slower rate of adsorption. The highest removal efficiency, approximately 84.1% for a 20 mg/L MG solution is recorded at 30 min, Therefore, it was chosen as the benchmark shaking time for further tests.

Table 2: BET results of Zn/Al@BOI

Parameter	Value	Method
BET area in m^2/g	80.53	BET method
Total pore volume in cm^3/g	0.186	BJH desorption
Average pore diameter in nm	3.77	BJH desorption (Dv(d))
type of Isotherm	Type IV	IUPAC classification
Hysteresis loop	H3	Indicates slit-shaped pores
Main pore size range (nm)	2–10	BJH desorption curve
Secondary pore range (nm)	20–60	Interparticle voids

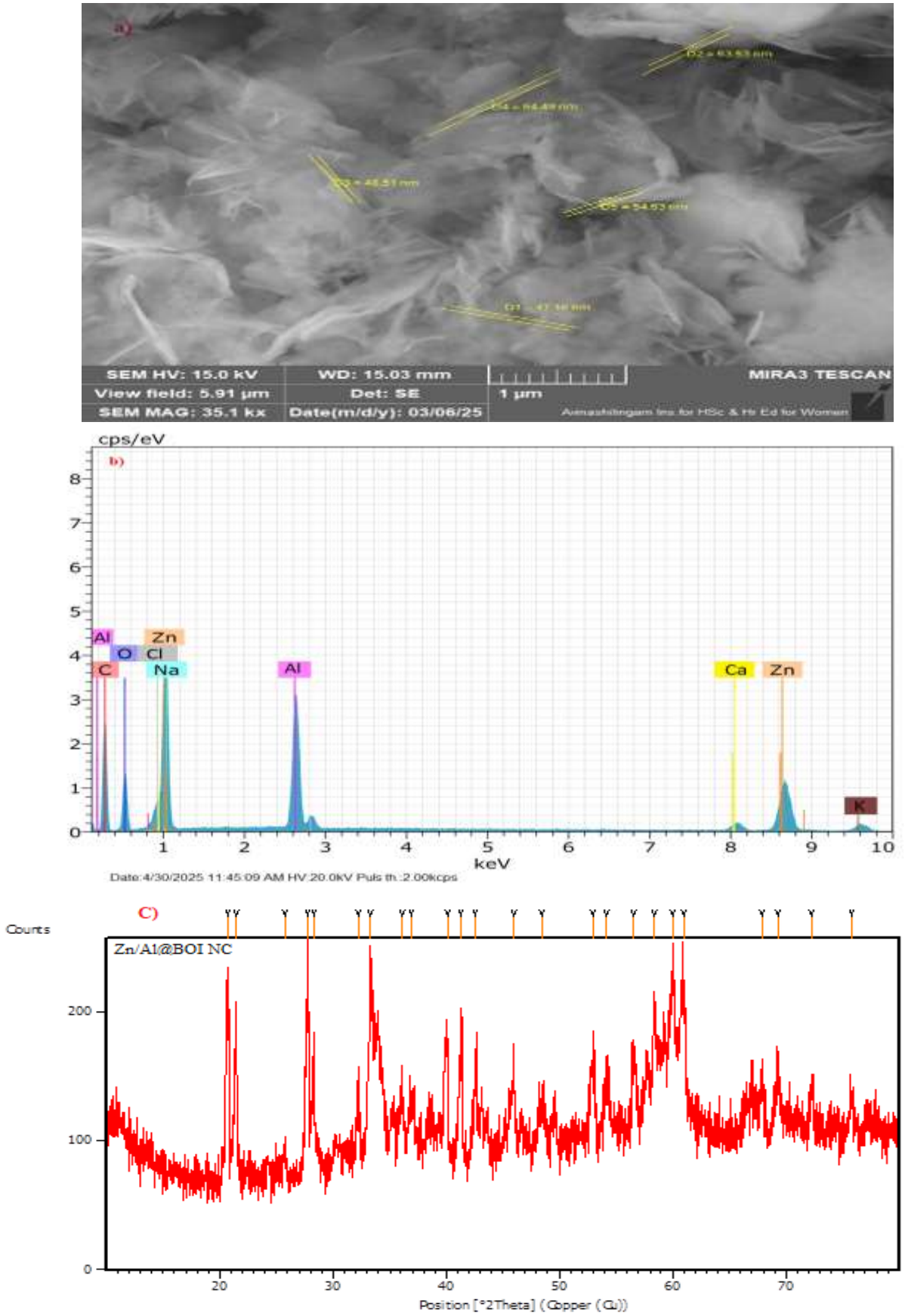

Fig. 2: (a) SEM, (b) EDX spectrum, (c) XRD pattern of the Zn/Al@BOI nanocomposite.

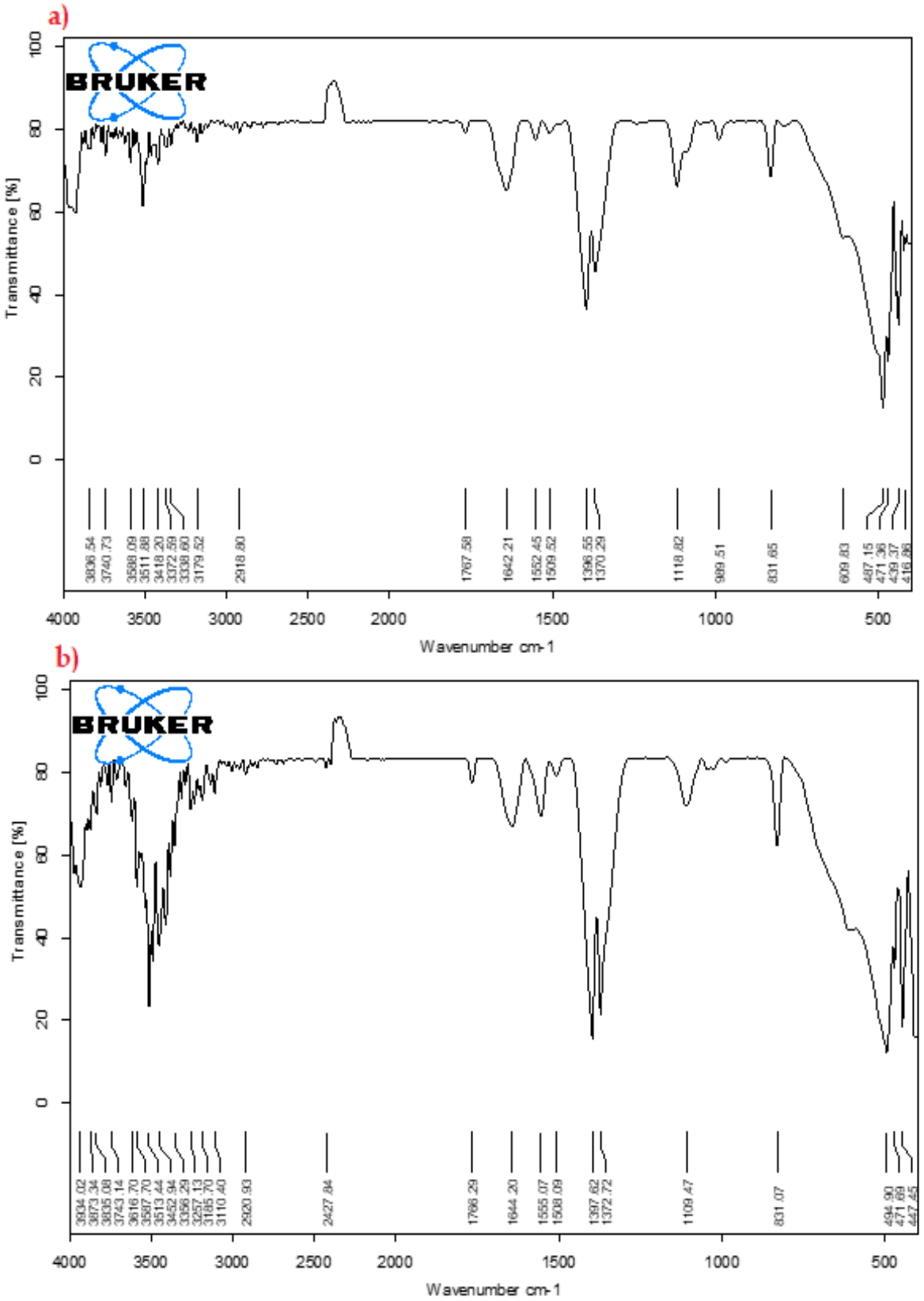

Fig. 3: FTIR profile of Zn/Al@BOI (a) before, (b) after MG dye adsorption

Fig. 7b illustrates the influence of nanocomposite dosage (0.08 to 0.6 g/L) at fixed pH-7, temperature-303 K, and time-30 min. The % improved with increased dosage due to the presence of numerous binding regions. The highest efficiency was achieved at 0.28 g/L, reaching 84.1% for 20 mg/L MG. Beyond this point, further

increases in dosage showed negligible improvements, likely due to particle agglomeration or overlapping of active sites, which can reduce effective surface area. Hence, 0.28 g/L was deemed the optimum dosage level. The role of pH was investigated by varying it from 2 to 9 (Fig. 7c), keeping temperature, contact time, and dosage constant at 303 K, 30 minutes, and 0.28 g/L, respectively. efficiency improved notably as pH increased, reaching a maximum of 86.3% at pH 8 for 20 mg/L MG. This trend is attributed to reduced competition from H^+ ions at higher pH levels and enhanced electrostatic attraction occurs between the negatively charged Zn/Al@BOI surface and cationic adsorbate. However, at lower pH, excess H^+ ions compete with dye molecules for active sites, reducing adsorption efficiency. Thus, pH 8 was identified as the optimum for further studies.

The interaction of temperature on adsorbate removal by Zn/Al@BOI was studied under optimal conditions—pH 8, 30 min contact time, and an optimum dosage level of 0.28 g/L (Fig. 7d). As temperature raised from 298 K to 318 K, adsorbate MG removal efficiency rose from 76.3% to 88.7% for a 20 mg/L MG solution. This improvement in adsorption efficiency confirms the endothermic nature of the process. Elevated temperatures facilitate dye diffusion by reducing solution viscosity and enhancing molecular mobility, which in turn improves penetration into mesoporous structures. Moreover, the increased thermal energy helps overcome the activation energy barrier associated with dye–surface interactions. Hence, 318 K was identified as the optimum temperature and was used for subsequent thermodynamic analysis.

Figure 7e illustrates how ranging the adsorbate MG concentration (10–100 mg/L) affects both the removal % and the adsorbate uptake (q_e), using the optimized conditions (pH 8, 318 K, 30 min, 0.28 g/L). As MG concentration increased, removal efficiency gradually declined—from approximately 98% at 10 mg/L to around 85% at 100 mg/L owing to the saturation of available active binding regions. Conversely, adsorption capacity rose significantly from ~49 mg/g to ~396 mg/g, reflecting enhanced mass transfer and dye availability at higher concentrations. This inverse relationship suggests that while low concentrations are optimal for high removal efficiency, higher concentrations boost the material's uptake capacity. These outcomes highlight the importance of tuning dye concentration on specific treatment goals and system requirements.

3.3. RSM Outcomes

A CCD involving 31 experimental runs was employed to systematically optimize the removal of MG dye by Zn/Al@BOI nanocomposite. This design enabled the investigation of four critical factors namely shaker time (A), nanocomposite dose (B), pH (C), and adsorbate MG concentration (D) to understand both their individual and combined influences on efficiency. Experimental replicates were incorporated to ensure statistical reliability and reduce variability. The model's validity and significance were evaluated using ANOVA (analysis of variance), with Fisher's F-test adopted to assess statistical relevance. Predictive accuracy was determined by R^2 measures how effectively the model captures the variability in the observed data. Table 3 presents the actual and coded values of all variables alongside the experimental results. The fitted quadratic regression equation, developed using the coded values of the variables are presented as follows:

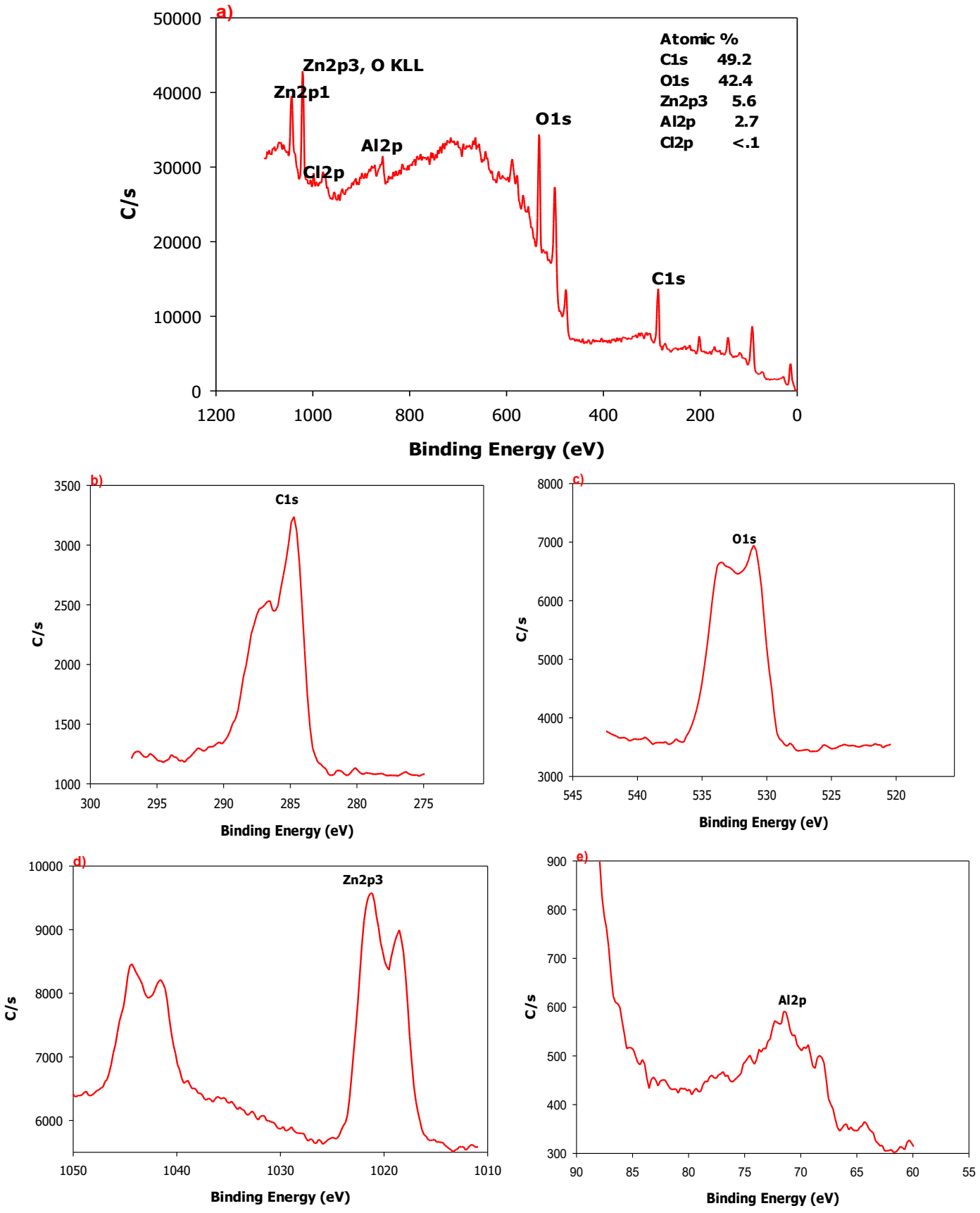

Fig. 4: XPS of Zn/Al@BOI. (a) Full range spectrum, (b) C1s, (c) O 1s, (d) Zn2p, (e) Al2p.

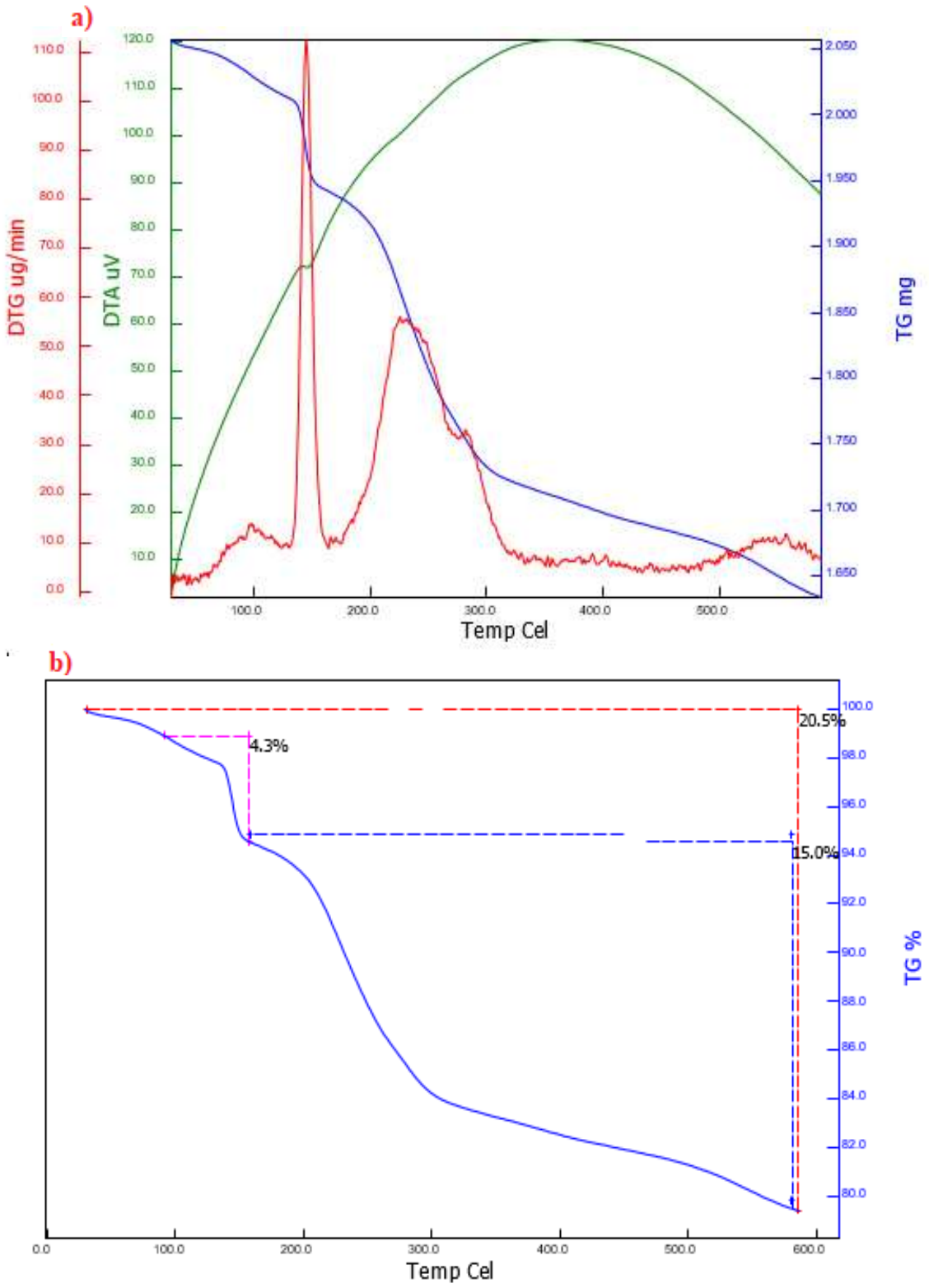

Fig. 5: (a) TGA–DTG–DTA plots and (B) TG curve of Zn/Al@BOI nanocomposite.

MG removal efficiency % = 96.5 + 1.80417 * A + 0.895833 * B - 0.0541667 * C - 1.49583 * D + 0.19375 * A*B + 0.00625 * A*C + 0.13125 * A*D - 0.08125 * B*C + 0.14375 * B*D - 0.01875 * C*D -2.80104 * A*A - 2.42604 * B*B - 5.16354 * C*C - 1.17604 * D*D (10)

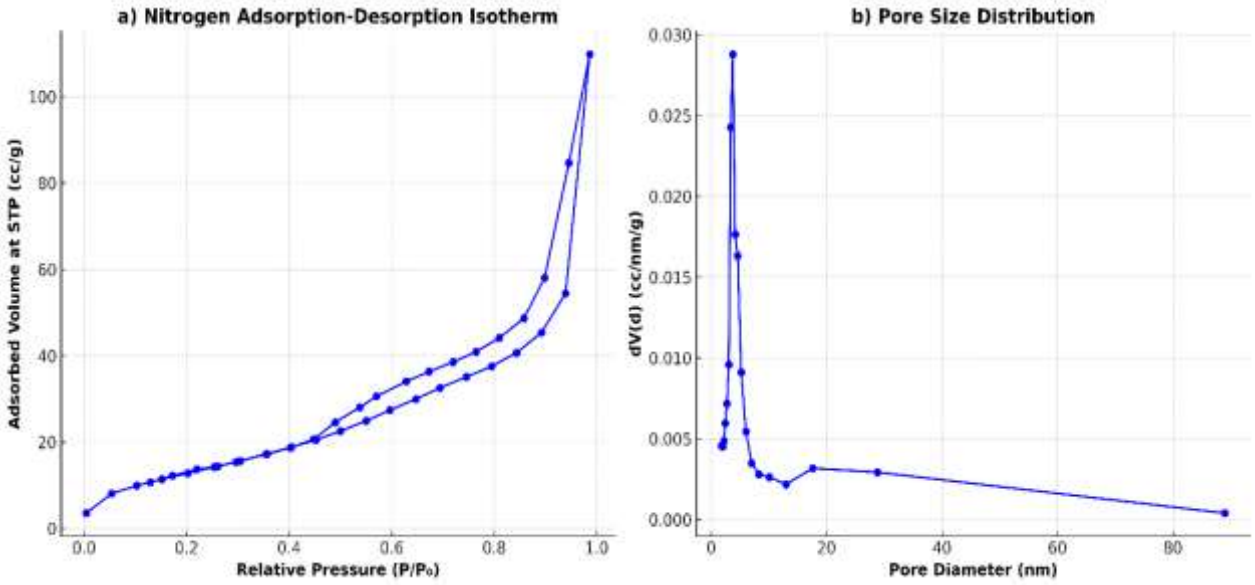

Fig. 6: Surface area and porosity analysis of Zn/Al@BOI: (a) Nitrogen sorption isotherm (BET), (b) BJH pore size distribution curve.

3.3.1. *ANOVA (Analysis of Variance)*

The ANOVA findings (Table 4) validate the statistical relevance of the quadratic model used in the study. A large F-value of 446.39 and a p-value under 0.0001 assess the model's strong predictive power and suitability. Among the linear factors, agitation time (A), adsorbent dosage (B), and initial MG concentration (D) significantly affected efficiency ($p < 0.0001$). However, pH (C) showed no notable influence on the process, with a p-value of 0.8893, suggesting its limited role in the studied range. The interaction terms (AC, AB, AD, BD, BC, and, CD) also returned p-values greater than 0.05, indicating that combined effects between these variables were statistically insignificant. On the other hand, the quadratic terms (A^2, B^2, C^2, D^2) were all highly significant ($p < 0.0001$), implying a pronounced curvature and a non-linear relationship between factors and response. The lack-of-fit was statistically insignificant ($p > 0.05$) and good R^2 value (0.9974) confirm strong agreement between experimental data and model predictions, explaining over 99% of the variation in MG (Table 5).

3.3.2. *RSM Plots and Interaction*

To assess MG dye adsorption onto Zn/Al@BOI, 3D plots were employed to examine the influences of agitation time, adsorbent dose, pH, and adsorbate MG concentration. As illustrated in Fig. 8(a) and 8(b), increasing agitation time enhanced MG removal, likely owing to the greater active binding regions early in the process. Adsorption approached equilibrium after 30 minutes as these sites became increasingly occupied. pH also played a key role, with MG removal rising from acidic to near-neutral pH and peaking at pH 8, as seen in Fig. 8(a) and 8(d). In strongly acidic conditions, H^+ ions likely competed with dye molecules for active regions, thereby diminishing the uptake ability. At elevated pH levels, deprotonation of surface groups can lead to electrostatic repulsion, slightly lowering dye uptake. Fig. 8(c) shows the interaction between dosage and dye concentration. While higher dosage improved removal due to more surface sites, increasing dye concentration (Fig. 8b, 8c) led to decreased efficiency as sites became saturated. This highlights the need to balance dosage with pollutant load.

Overall, the response plots reveal that all parameters influence each other and must be optimized collectively for efficient MG degradation.

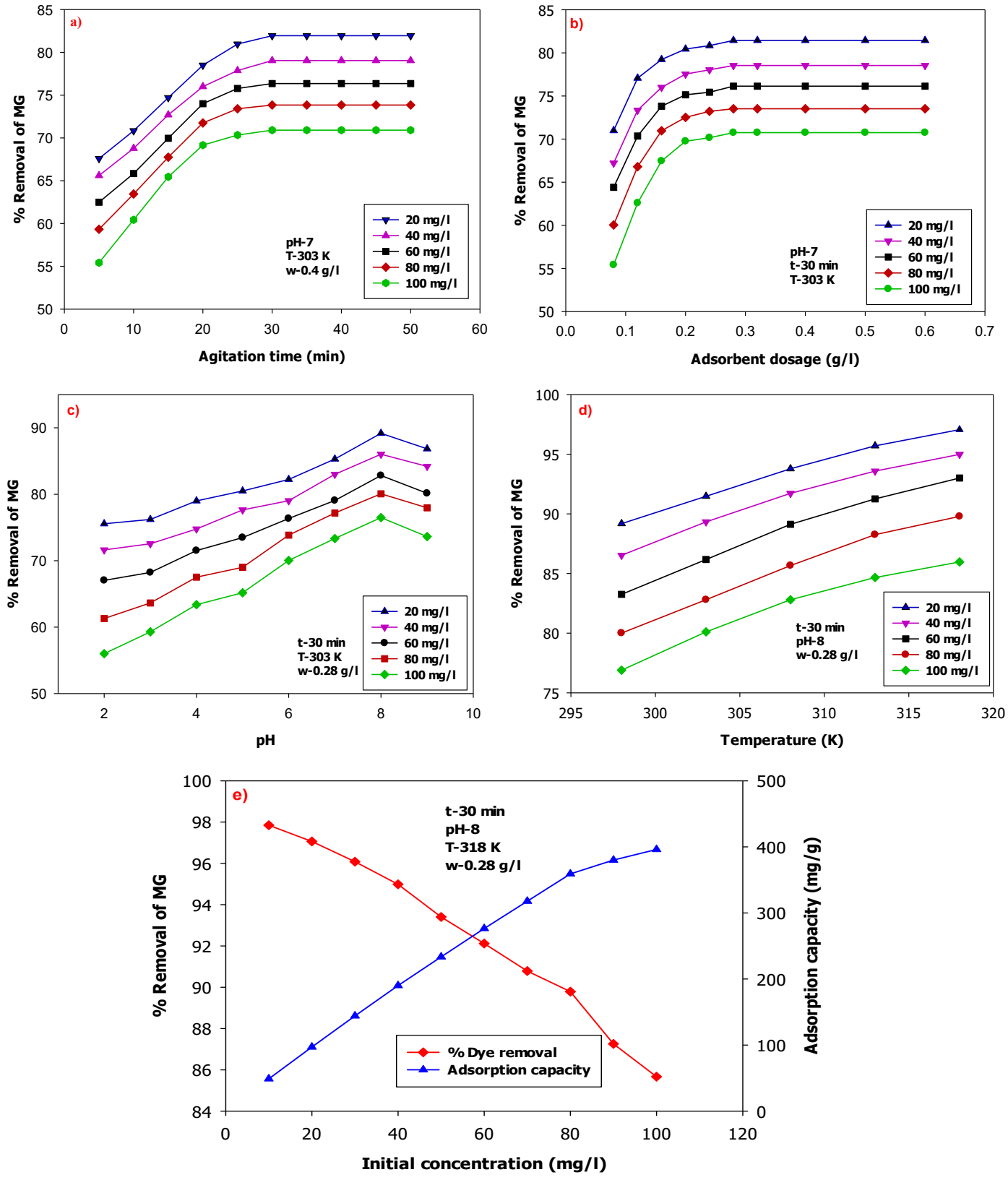

Fig. 7: Optimization of key operational variables on MG by Zn/Al@BOI: (a) time, (b) dosage, (c) pH, (d) temperature, and (e) initial concentration vs. q_e

3.3.3. Optimization

This study aimed to establish the optimal inputs for maximum MG degradation using Design-Expert 13 software. The suggested parameters like agitation time of 33.1 min, nanocomposite dosage of 0.3 g/L, pH 7.9, and adsorbate MG concentration of 20 mg/L, predicted a removal efficiency of 96.87% with a desirability of 0.994 (Fig. 9). Experimental validation under given inputs closely matched the calculated outcome, confirming the model's accuracy.

Table 3: Designed factors using CCD.

Run	A:Time(min)	B:Dose(g/l)	C:pH	D:Concentration (mg/l)	MG Removal efficiency %
1	30	0.3	8	20	96.5
2	40	0.2	7	25	84
3	30	0.3	6	20	76
4	40	0.4	9	15	89
5	20	0.2	9	25	80.4
6	30	0.3	10	20	76.1
7	10	0.3	8	20	82
8	30	0.3	8	20	96.5
9	20	0.2	7	25	80.5
10	20	0.4	9	15	85
11	40	0.2	7	15	87
12	50	0.3	8	20	89
13	30	0.1	8	20	85.5
14	40	0.2	9	15	87
15	40	0.2	9	25	84
16	30	0.3	8	20	96.5
17	20	0.4	7	25	82.4
18	20	0.4	7	15	85.5
19	20	0.2	7	15	84
20	20	0.4	9	25	82.2
21	30	0.5	8	20	88.5
22	40	0.4	7	15	89.1
23	30	0.3	8	20	96.5
24	30	0.3	8	20	96.5
25	30	0.3	8	20	96.5
26	30	0.3	8	20	96.5
27	40	0.4	7	25	86.9
28	20	0.2	9	15	84
29	30	0.3	8	10	95
30	30	0.3	8	30	89
31	40	0.4	9	25	86.3

Table 4: ANOVA Output for the Fitted Quadratic Model

Source	Sum of Squares	df	Mean Square	F-value	p-value	
Model	1171.46	14	83.68	446.39	< 0.0001	significant
A-Time	74.55	1	74.55	397.73	< 0.0001	
B-Dosage	21.09	1	21.09	112.53	< 0.0001	
C-pH	0.0038	1	0.0038	0.0200	0.8893	
D-Concentration	69.70	1	69.70	371.84	< 0.0001	
AB	0.2756	1	0.2756	1.47	0.2429	
AC	0.0506	1	0.0506	0.2701	0.6104	
AD	0.6006	1	0.6006	3.20	0.0924	
BC	0.0056	1	0.0056	0.0300	0.8646	
BD	0.1056	1	0.1056	0.5635	0.4638	
CD	0.1056	1	0.1056	0.5635	0.4638	
A^2	229.39	1	229.39	1223.76	< 0.0001	
B^2	172.67	1	172.67	921.16	< 0.0001	
C^2	771.68	1	771.68	4116.77	< 0.0001	
D^2	26.21	1	26.21	139.80	< 0.0001	
Residual	3.00	16	0.1874			
Lack of Fit	3.00	10	0.2999			
Pure Error	0.0000	6	0.0000			
Cor Total	1174.46	30				

Table 5: Model fit evaluation criteria

Std. Dev.	0.4330
Mean	87.64
C.V. %	0.4940
R^2	0.9974
Adjusted R^2	0.9852
Predicted R^2	0.9753
Adeq Precision	59.0789

3.4. Adsorption isotherms

MG adsorption onto Zn/Al@BOI was applied to evaluate the Langmuir and Freundlich isotherm models (Fig. 10a–b). The Langmuir model (R^2 = 0.9787) uniform surface adsorption forming a mono-layer of adsorbate molecules, with a high maximum capacity of 376 mg/g—likely due to electrostatic interactions and active surface sites. However, the Freundlich model showed an even better fit (R^2 = 0.9957), pointing to non-uniform surface characteristics supporting multi-layer adsorption. The Freundlich constant (n = 1.9055) confirmed favorable adsorption. These results imply that while Langmuir highlights high capacity, the Freundlich model more

accurately describes the adsorption behavior of the doped bio-waste-based material (Sowjanya et al. 2023; Ratnam et al. 2022)

3.5. Adsorption Kinetics

To elucidate the nature of the adsorption interaction kinetics of MG onto Zn/Al@BOI, Observed data were interpreted through pseudo-first and -second order models (Fig. 10c–d), with corresponding kinetic parameters mentioned in Table 6. The pseudo-first order model (Fig. 10c) offered a weaker correlation (R^2 = 0.8920), indicating limited suitability. Conversely, the pseudo-2nd-order model (Fig. 10d) modeled the data exceptionally well (R^2 = 0.9998), highlighting chemisorption as the dominant mechanism. This suggests that the adsorption process involves electron sharing or exchange through valence forces, with surface complexation or ion exchange as the rate-determining steps. Such behavior aligns with the highly active and heterogeneous surface of Zn/Al@BOI, making it efficient for MG removal (Ratnam et al. 2022; Subhashita et al. 2022).

3.6. Thermodynamic studies

Thermodynamic variables for MG removal onto Zn/Al@BOI were determined using the van't Hoff plot (Fig. 10e), which exhibited strong linearity (R^2 = 0.9716), confirming a clear temperature dependence. The enthalpy change (ΔH° = +23.82 kJ/mol) suggests the process is endothermic, likely involving chemisorption or diffusion through pores. An entropy change (ΔS° = +103.49 J/(mol·K)) signifies enhanced disorder at the adsorbent–MG dye boundary, possibly owing to moisture evaporation and rearrangement of the adsorbate structure. Gibbs free energy outcomes (ΔG° = –9.10, –8.57, and –8.10 kj/mol at 318, 313, and 308 K, respectively) confirm the spontaneity and thermodynamic favorability of the process. The improved removal at higher temperatures may result from enhanced dye molecule mobility and easier access to active binding sites on the adsorbent (Sowjanya et al. 2023; Ratnam et al. 2022; Subhashita et al. 2022).

Table 6: Kinetic variables of removal of MG onto Zn/Al@BOI

S.No	Model	Parameters
1	Pseudo-1st -order model	q_e=43.77 mg.g^{-1}
		R^2=0.8920
2	Pseudo -2nd -order model	q_e= 444 mg.g^{-1}
		R^2=0.9998
3	Elovich model	R^2=0.9115
4	Intra particle diffusion	R^2=0.92

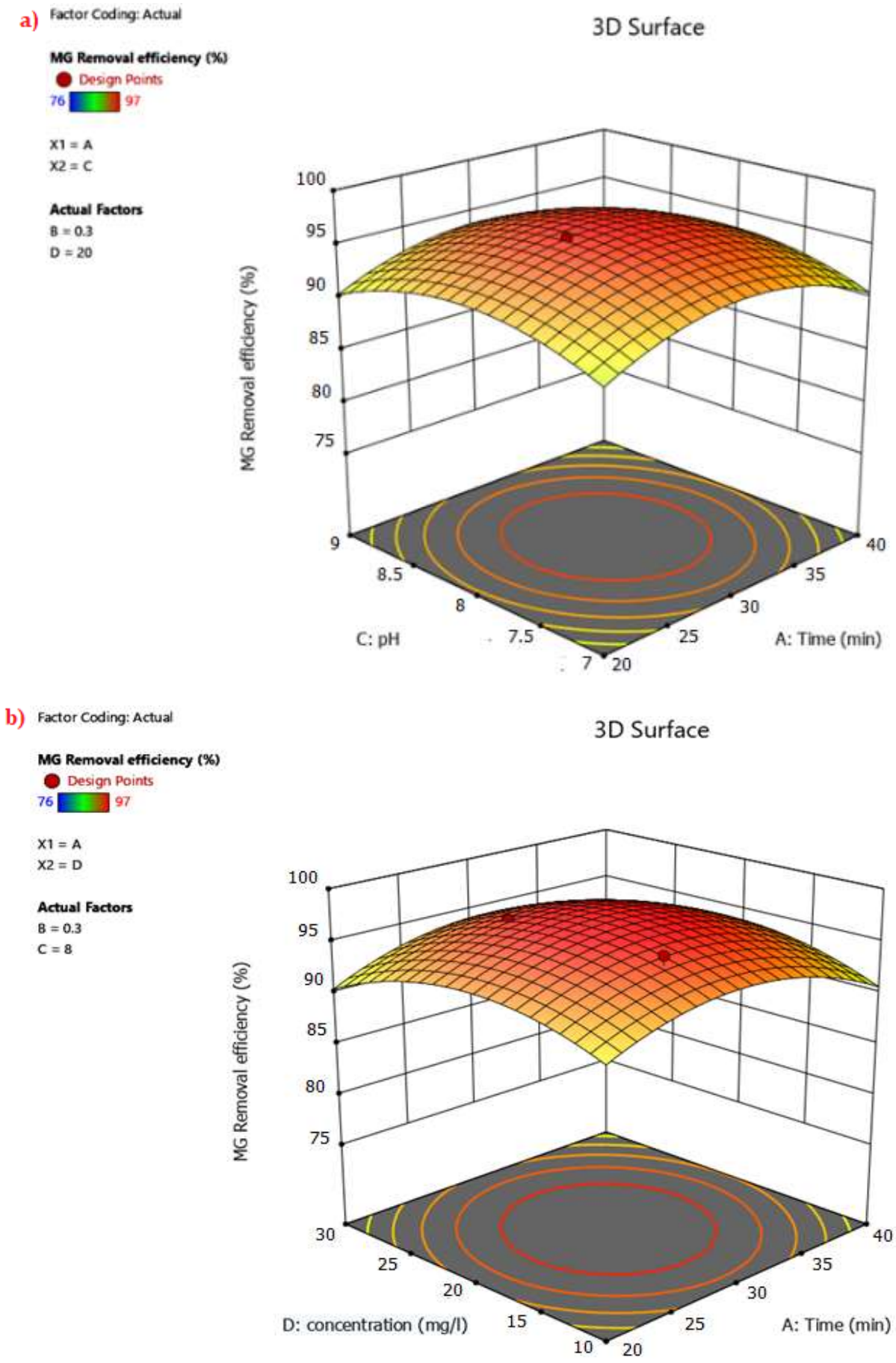

Fig. 8. Continued

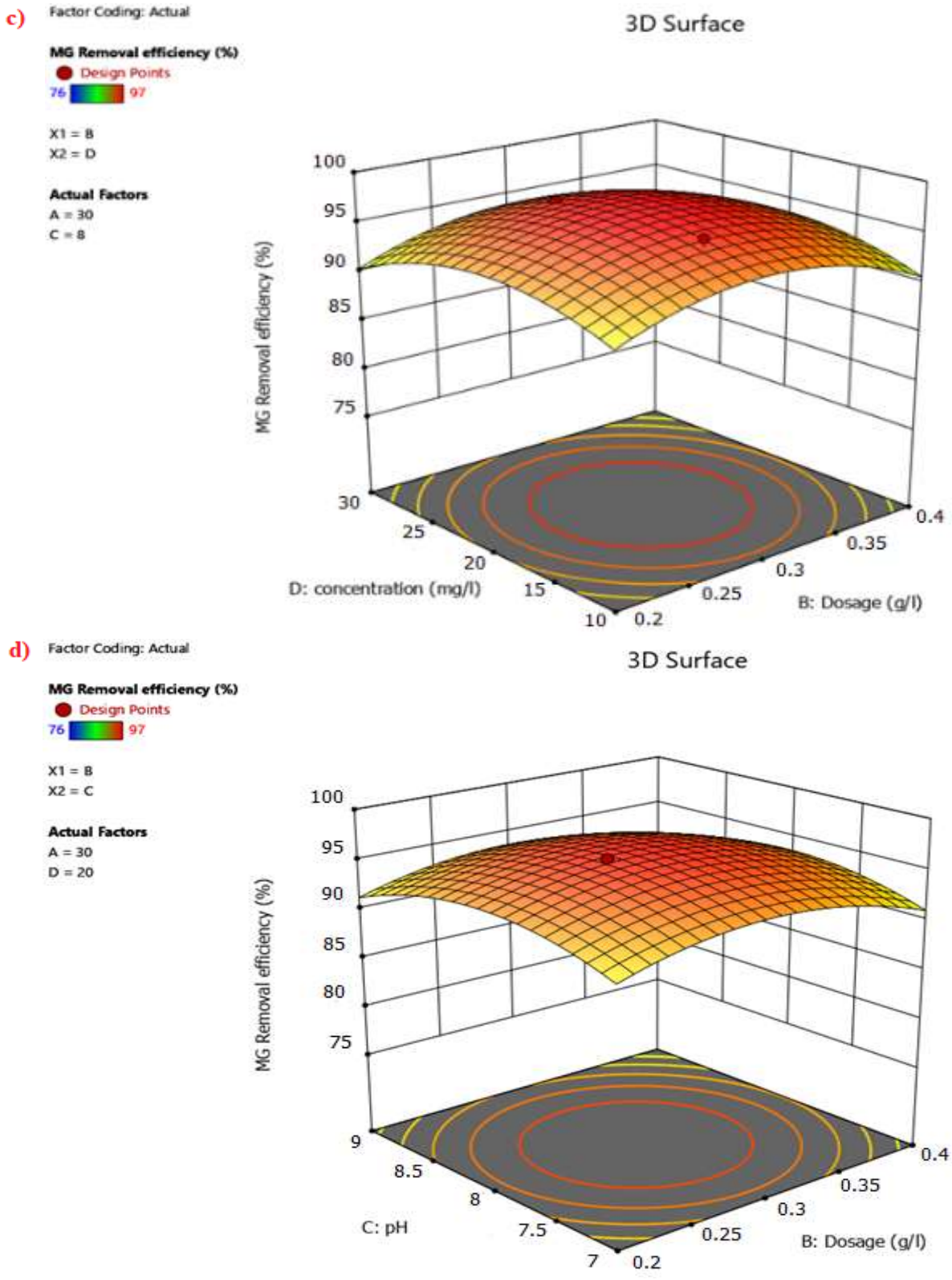

Fig. 8: Three-dimensional surface graphs showing the combined effects of key inputs on adsorbate onto Zn/Al@BOI: (a) solution pH and time, (b) adsorbate concentration and time, (c) concentration and nanocomposite dosage, and (d) pH and dosage.

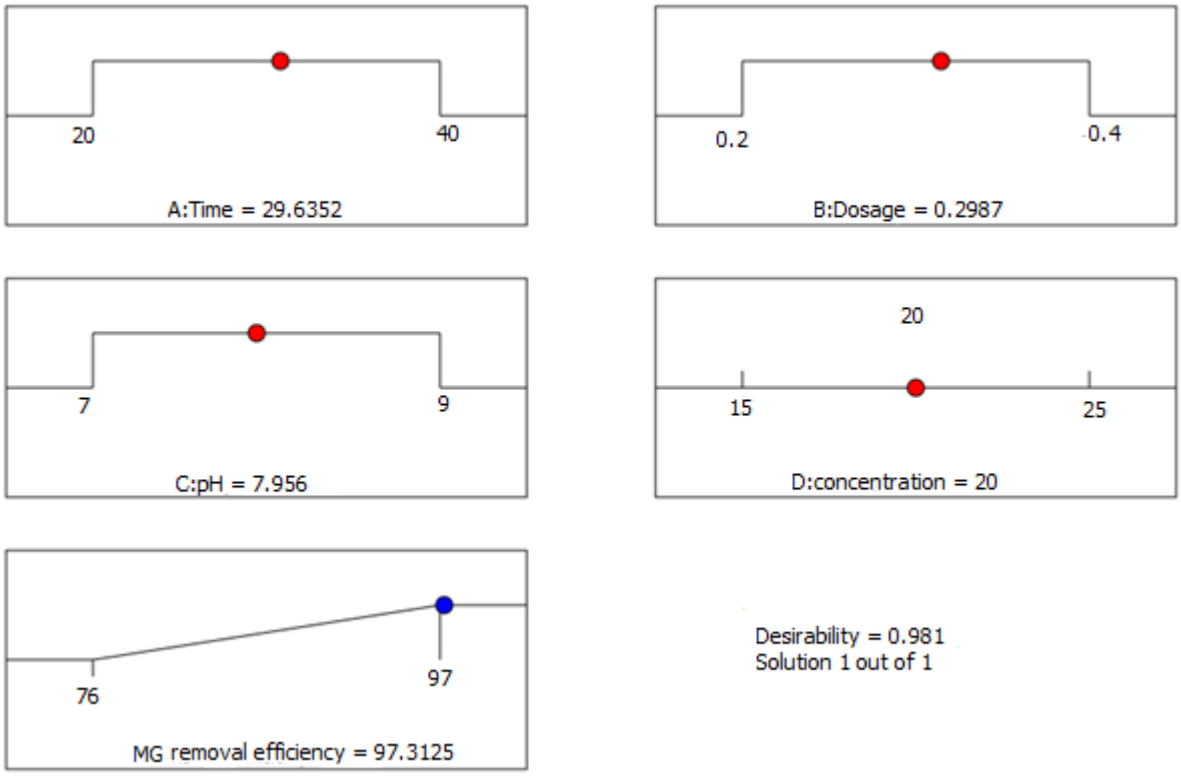

Fig. 9: Ramp plot of optimization.

4.CONCLUSIONS

In this work, a green co-precipitation approach was utilized to synthesize a zinc and aluminum dually doped nanocomposite derived from Brassica oleracea var. italica stem bio-waste (Zn/Al@BOI) for efficient malachite green (MG). Characterization analysis including SEM-EDX, XRD, FTIR, XPS, TGA, and, BET revealed a well-developed crystalline structure, heterogeneous surface morphology, excellent thermal stability, and a marked surface area of 80.53 $m^2.g^{-1}$. EDX and XPS analyses confirmed the integration of Zn and Al into the bio-waste matrix, while FT-IR spectra highlighted functional groups involved in dye interaction. Process inputs optimization was carried out using RSM with a CCD, identifying ideal conditions, agitation time of 29.64 min, dose of 0.2987 g/L, pH 7.96, and MG concentration of 20 mg/L, resulting in 97.31% removal under optimized inputs. The Langmuir isotherm estimated a maximum uptake capacity of 336 $mg.g^{-1}$, that closely matched the experimental result of around 356 mg/g. Kinetic studies noted that the adsorption followed a pseudo-2nd-order model, while thermodynamic study confirmed the approach was spontaneous, endothermic and primarily driven by physisorption. These results highlight Zn/Al@BOI as an efficient, sustainable, and affordable material for water purification.

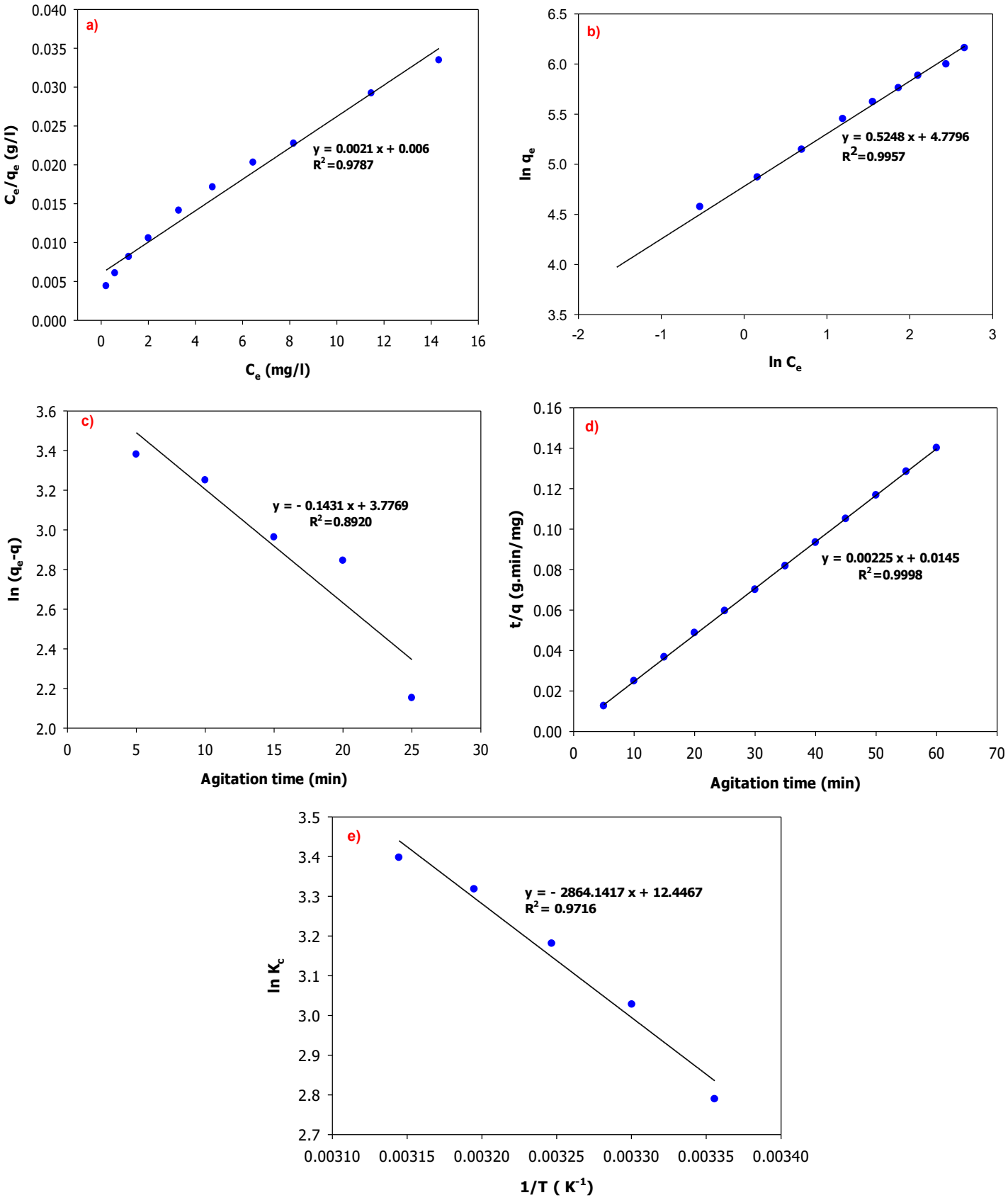

Fig. 10: (a) Langmuir isotherm, (b) Freundlich isotherm, (c) pseudo-1st order model, (d) pseudo-2nd order model, and (e) Van't Hoff plot for MG uptake onto Zn/Al@BOI

Author Contributions: Yagna Sri Thikkada, NagaRaju Yendluri and Kapavarapu Sreekar handled data preparation, assessment, experimentation and computation. **Pulipati King** and **Meena Vangalapati** contributed to research planning, research approach, project administration and mentorship. **Alpitha Suhasini Juttuka and Venkata Ramana Avula** supported to resource facilitation and securing external support.

Funding: The authors did not receive any specific funding for this work.

Acknowledgments: The authors sincerely thank the Department of Chemical Engg., AU College of Engg, for providing the necessary research facilities and academic support throughout the study.

Conflicts of Interest: No competing financial interests have been declared by the authors.

REFERENCES

1. Ananda, A. Ramakrishnappa, T. Ravishankar, T.N. Reddy Yadav, L.S. Jayanna, B.K. (2023). RSM-BBD optimization approach for degradation and electrochemical sensing of Evan's blue dye using green synthesized ZrO_2–ZnO nanocomposite. Inorg. Nano-Met. Chem. https://doi.org/10.1080/24701556.2023.2204632.
2. Ashraf, I. Singh, N.B. Agarwal, A. (2023). Green synthesis of iron oxide nanoparticles using Amla seed for methylene blue from water. Mater. Today Proc. 72, 311–316. https://doi.org/10.1016/j.matpr.2022.07.096.
3. Aziz, T. Farid, A. Chinnam, S. Haq, F. Kiran, M. Wani, A.W. Akhtar, M.S. (2023). Modified cellulose nanocrystals for cationic dye adsorption. Chemosphere 321, 137999. https://doi.org/10.1016/j.chemosphere.2023.137999.
4. Banerjee, S. Chattopadhyaya, M.C. (2017). Tartrazine removal from aqueous solutions using agricultural by-products. Arab. J. Chem. 10, S1629–S1638. https://doi.org/10.1016/j.arabjc.2013.06.005.
5. Barik, S. Behera, L. Badamali, S.K. (2017). Thermal and antimicrobial properties of PAN/Zn-Al LDH nanocomposites. Compos. Interfaces 24, 579–591. https://doi.org/10.1080/09276440.2017.1317714.
6. Bilal, M. Ihsanullah, I. Shah, M.U.H. Reddy, A.V.B. Aminabhavi, T.M. (2022). Recent advances in the removal of dyes from wastewater using low-cost adsorbents. J. Environ. Manage. 321, 115981. https://doi.org/10.1016/j.jenvman.2022.115981.
7. Chan, Y.Y. Pang, Y.L. Lim, S. et al. (2020). Biosynthesized Fe- and Ag-doped ZnO nanoparticles using Clitoria ternatea Linn extract for Congo red degradation. Environ. Sci. Pollut. Res. 27, 34675–34691. https://doi.org/10.1007/s11356-020-09812-8.
8. Çifçi, D.İ. Aydın, N. (2022). Magnetic iron-doped filtered coffee bio-waste-based carbon for the adsorption of reactive blue 21. J. Water Chem. Technol. 44, 317–326. https://doi.org/10.3103/S1063455X22050050.
9. Debord, J. Harel, M. Bollinger, J.C. Chu, K.H. (2022). The Elovich isotherm equation: Back to the roots and new developments. Chem. Eng. Sci. 262, 118012. https://doi.org/10.1016/j.ces.2022.118012.
10. Dharmarathna, S.P. Priyantha, N. (2024). Investigation of boundary layer effect of intra-particle diffusion on methylene blue adsorption. Energy Nexus 14, 100294. https://doi.org/10.1016/j.nexus.2024.100294.
11. Dutta, S. Gupta, B. Srivastava, S.K. Gupta, A.K. (2021). Recent advances on the removal of dyes from wastewater using various adsorbents: A critical review. Mater. Adv. 2, 4497–4531. https://doi.org/10.1039/d1ma00190j.
12. El Naeem, G.A. Abd-Elhamid, A.I. Farahat, O.O. El-Bardan, A.A. Soliman, H.M. Nayl, A.A. (2022). Crystal violet and methylene blue adsorption using sugarcane bagasse cellulose adsorbent. J. Mater. Res. Technol. 19, 3241–3254. https://doi.org/10.1016/j.jmrt.2022.06.112.
13. El Ouadhriri, F. Adachi, A. Elyemni, M. Bayout, A. Hmamou, A. Bendaoud, A. Lahkimi, A. (2022). N, P-dually doped carbocatalyst from olive pomace obtained by hydrothermal carbonization. J. Environ. Chem. Eng. 10, 108449. https://doi.org/10.1016/j.jece.2022.108449.

14. Elizalde-González, M.P. Geyer, W. Guevara-Villa, M.R. Mattusch, J. Peláez-Cid, A.A. Wennrich, R. (2006). Maize waste adsorbent for textile. Colloids Surf. A 278, 89–97. https://doi.org/10.1016/j.colsurfa.2005.12.043. Granado-Castro, M.D. Galindo-Riaño, M.D. Gestoso-Rojas, J. Sánchez-Ponce, L. Casanueva-Marenco, M.J. Díaz-de-Alba, M. (2024). Ecofriendly application of calabrese broccoli stalk waste for Pb^{2+} removal. Agronomy 14, 554. https://doi.org/10.3390/agronomy14030554. Ho, Y.S. McKay, G. (1999). Pseudo-second order model for sorption processes. Process Biochem. 34, 451–465. https://doi.org/10.1016/S0032-9592(98)00112-5.
15. Inobeme, A. Mathew, J.T. Adetunji, C.O. Agbugui, M.O. Inobeme, J. Enerijiofi, K.E. Daniel, O. (2024). Understanding dye pollution and its impact on the environment. In: Dye Pollution from Textile Industry. Springer, Singapore, pp. 3–15. https://doi.org/10.1007/978-981-99-2262-0_1.
16. Javadian, H. Angaji, M.T. Naushad, M. (2014). Polyaniline/γ-alumina nanocomposite for anionic dye adsorption. J. Ind. Eng. Chem. 20, 3890–3900. https://doi.org/10.1016/j.jiec.2013.12.032.
17. Jha, A. Mishra, S. (2024). Exploring the potential of waste biomass-derived pectin and its functionalized derivatives for water treatment. Int. J. Biol. Macromol. 133613. https://doi.org/10.1016/j.ijbiomac.2024.133613.
18. Kacan, E. (2016). Activated carbon from textile sludge for. J. Environ. Manage. 166, 116–123. https://doi.org/10.1016/j.jenvman.2015.10.003.
19. Karunakaran, G. Cho, E.B. Kumar, G.S. Kolesnikov, E. Govindaraj, S.K. Mariyappan, K. Boobalan, S. (2023). CTAB enabled microwave-hydrothermal assisted mesoporous Zn-doped hydroxyapatite nanorods synthesis using bio-waste Nodipecten nodosus scallop. Environ. Res. 216, 114683. https://doi.org/10.1016/j.envres.2022.114683.
20. Klett, C. Barry, A. Balti, I. Lelli, P. Schoenstein, F. Jouini, N. (2014). Nickel-doped ZnO for methyl orange and tartrazine adsorption. J. Environ. Chem. Eng. 2, 914–926. https://doi.org/10.1016/j.jece.2014.02.014.
21. Li, X. Wang, Z. Ning, J. Gao, M. Jiang, W. Zhou, Z. Li, G. (2018). Polyethyleneimine-modified persimmon tannin bioadsorbent for anionic dye adsorption. J. Environ. Manage. 217, 305–314. https://doi.org/10.1016/j.jenvman.2018.03.103.
22. Liu, J. Wang, N. Zhang, H. Baeyens, J. (2019). Adsorption of Congo red dye on $FexCo_{3-x}O_4$ nanoparticles. J. Environ. Manage. 238, 473–483. https://doi.org/10.1016/j.jenvman.2019.03.007.
23. Mall, I.D. Srivastava, V.C. Kumar, G.V.A. Mishra, I.M. (2006). Mesoporous fertilizer plant waste carbon for dye adsorption. Colloids Surf. A 278, 175–187. https://doi.org/10.1016/j.colsurfa.2005.12.046.
24. Manojkumar, U. Kaliannan, D. Srinivasan, V. Balasubramanian, B. Kamyab, H. Mussa, Z.H. Palaniyappan, J. Mesbah, M. Chelliapan, S. Palaninaicker, S. (2023). Green synthesis of zinc oxide nanoparticles using Brassica oleracea var. botrytis leaf extract. Chemosphere 323, 138204. https://doi.org/10.1016/j.chemosphere.2023.138204.
25. Monvisade, P. Siriphannon, P. (2009). Chitosan intercalated montmorillonite for cationic dye adsorption. Appl. Clay Sci. 42, 427–431. https://doi.org/10.1016/j.clay.2008.04.005.
26. Ouassif, H. Moujahid, E.M. Lahkale, R. Sadik, R. Bouragba, F.Z. Sabbar, E.M. Diouri, M. (2020). Zinc–aluminum layered double hydroxide for tartrazine. Surf. Interfaces 18, 100401. https://doi.org/10.1016/j.surfin.2019.100401.
27. Parveen, K. Rafique, U. (2018). Cobalt-doped alumina hybrids for textile effluent adsorption. Adsorpt. Sci. Technol. 36, 182–197. https://doi.org/10.1177/0263617418775014.
28. Poiba, V.R. Sowjanya, B. King, P. Vangalapati, M. (2023). Removal of methylene blue dye by using synthesised Grevillea robusta silver nanoparticles. Adv. Mater. Process. Technol. 1–15. https://doi.org/10.1080/2374068X.2023.2197939.
29. Polipalli, K. Pulipati, K. (2013). Equilibrium, kinetic and thermodynamic studies of biosorption of methylene blue dye using plant biomass as biosorbent. Int. J. Sci. Eng. Res. 4, 1244–1252.

30. Raj, R.M. Ganesan, S. Suganthi, S. Vignesh, S. Hatamleh, A.A. Alnafisi, B.K. Lo, H.M. (2023). Zinc–aluminium polymeric framework for drug and. Chemosphere 311, 137105. https://doi.org/10.1016/j.chemosphere.2022.137105.
31. Ratnam, M.V. Vangalapati, M. Rao, K.N. Chandra, K.R. (2022). Efficient removal of methyl orange using MgO nanoparticles loaded onto activated carbon. Bull. Chem. Soc. Ethiop. 36, 531–544. https://doi.org/10.4314/bcse.v36i3.13.
32. Raval, N.P. Shah, P.U. Shah, N.K. (2017). Malachite green 'a cationic dye' and its removal from aqueous solution by adsorption. Appl. Water Sci. 7, 3407–3445. https://doi.org/10.1007/s13201-016-0511-7.
33. Shindhal, T. Rakholiya, P. Varjani, S. Pandey, A. Ngo, H.H. Guo, W. Taherzadeh, M.J. (2021). A critical review on advances in the practices and perspectives for the treatment of dye industry wastewater. Bioengineered 12, 70–87. https://doi.org/10.1080/21655979.2020.1863035.
34. Sowjanya, B. King, P. Meena, V. (2023). Skin of Allium sativum mediated green synthesis of ZnO nanoparticles for Congo red. Eur. Chem. Bull. 13, 326–332. https://doi.org/10.48047/ecb.13.05.055.
35. Sowjanya, B. King, P. Vangalapati, M. Myneni, V.R. (2023). Copper-doped zinc oxide nanoparticles: Synthesis, characterization, and application for adsorptive removal of toxic azo dye. Int. J. Chem. Eng. 2023, 8640288. https://doi.org/10.1155/2023/8640288.
36. Sowjanya, B. Sirisha, U. Juttuka, A.S. Matla, S. King, P. Vangalapati, M. (2022). Synthesis and characterization of zinc oxide nanoparticles: Application for alizarin red S. Mater. Today Proc. 62, 3968–3972. https://doi.org/10.1016/j.matpr.2022.02.004.
37. Subhashita, M. Punugoti, T. Sowjanya, B. Poiba, V.R. Vangalapati, M. (2022). Synthesis of Cu/ZnO nanoparticles and their use for Cetrimonium Bromide removal. Adv. Mater. Process. Technol. 8, 1880–1888. https://doi.org/10.1080/2374068X.2022.2087075.
38. Tajat, N. El Hayaoui, W. Bougdour, N. Idlahcen, A. Radaa, C. Bakas, I. Qourzal, S. (2022). Utilization of Zn–Al–Cl layered double hydroxide as an adsorbent for the removal of anionic dye Remazol Red 23. Nanotechnol. Environ. Eng. 7, 343–357. https://doi.org/10.1007/s41204-022-00200-6.
39. Velusamy, S. Kandasamy, K. Kuppusamy, M.R. Manikandan, M. Velusami, N. Govindasamy, K. (2025). Eco-friendly green synthesis: Harnessing Ni/Al-layered double hydroxide-activated carbon nanocomposite. Int. J. Environ. Res. 19, 1–18. https://doi.org/10.1007/s41742-025-00530-2.
40. Verma, A. Thakur, S. Mamba, G. Gupta, R.K. Thakur, P. Thakur, V.K. (2020). Graphite modified sodium alginate hydrogel composite for efficient removal of malachite green dye. Int. J. Biol. Macromol. 148, 1130–1139. https://doi.org/10.1016/j.ijbiomac.2020.01.155.
41. Youssef, A.M. Moustafa, H.A. Barhoum, A. Hakim, A.E.F.A. Dufresne, A. (2017). Polyaniline nanocomposite based on Zn/Al-LDHs: Morphological, electrical and antibacterial evaluation. ChemistrySelect 2, 8553–8566. https://doi.org/10.1002/slct.201701312.
42. Zhang, H. Xing, L. Liang, H. Ren, J. Ding, W. Wang, Q. Xu, C. (2022). Efficient removal of Remazol Brilliant Blue R from water by a cellulose-based activated carbon. Int. J. Biol. Macromol. 207, 254–262. https://doi.org/10.1016/j.ijbiomac.2022.03.057.